Mon. Not. R. Astron. Soc. **328,** 266–276 (2001)

Scattered light models of the dust shell around HD 179821

T. M. Gledhill★ and M. Takami
Department of Physical Sciences, University of Hertfordshire, College Lane, Hatfield, Hertfordshire AL10 9AB

Accepted 2001 July 27. Received 2002 July 26; in original form 2001 February 28

ABSTRACT

The dust shell around the evolved star HD 179821 has been detected in scattered light in near-IR imaging polarimetry observations. Here, we subtract the contribution of the unpolarized stellar light to obtain an intrinsic linear polarization of between 30 and 40 per cent in the shell that seems to increase with radial offset from the star. The *J*- and *K*-band data are modelled using a scattering code to determine the shell parameters and dust properties. We find that the observations are well described by a spherically-symmetric distribution of dust with an r^{-2} density law, indicating that when mass-loss was occurring, the mass-loss rate was constant. The models predict that the detached nature of a spherically-symmetric, optically-thin dust shell, with a distinct inner boundary, will only be apparent in polarized flux. This is in accordance with the observations of this and other optically-thin circumstellar shells, such as IRAS 17436+5003. By fitting the shell brightness we derive an optical depth to the star that is consistent with *V*-band observations and that, assuming a distance of 6 kpc, gives an inner-shell radius of $r_{\rm in} = 1.44 \times 10^{15}$ m, a dust number density of $N_{\rm in} = 2.70 \times 10^{-1}\,{\rm m}^{-3}$ at $r_{\rm in}$ and a dust mass of $M_{\rm d} = 0.08\,{\rm M}_{\odot}$. We have explored axisymmetric shell models but conclude that any deviations from spherical symmetry in the shell must be slight, with an equator-to-pole density contrast of less than 2:1. We have not been able to fit simultaneously the high linear polarizations and the small $[E(J-K) = -0.3]$ colour excess of the shell and we attribute this to the unusual scattering properties of the dust. We suggest that the dust grains around HD 179821 either are highly elongated or consist of aggregates of smaller particles.

Key words: polarization – scattering – stars: AGB and post-AGB – circumstellar matter – stars: individual: HD 179821 – infrared: stars.

1 INTRODUCTION

The evolved star HD 179821 (IRAS 19114+0002) is surrounded by a dusty circumstellar envelope detectable in scattered light out to a radius of at least 9 arcsec (Kastner & Weintraub 1995; Ueta, Meixner & Bobrowsky 2000). Mid-IR imaging (Hawkins et al. 1995) shows that the warm dust is distributed in a shell around the star with an inner boundary at a radius of 1.75 arcsec (Jura & Werner 1999). There appears to be little or no dust inside this inner boundary, suggesting that the mass-loss terminated some time ago. The detached nature of the shell was also indicated by earlier ground-based and *IRAS* photometry, which showed the double-peaked profile characteristic of emission from a hot photosphere and warm dust shell (Hrivnak, Kwok & Volk 1989, hereafter HKV89).

It is still not clear whether HD 179821 is a low- or intermediate-mass post-AGB star or a more massive supergiant (see Reddy & Hrivnak 1999 for a review of the arguments, also Thévenin, Parthasarathy & Jasniewicz 2000). This fundamental uncertainty is reflected in the wide range of estimates of the distance to the star (between 1.5 and 6 kpc) and the quantities dependent upon it, such as the physical size of the shell and the mass of dust contained. If the star is in the post-AGB phase then the object is a proto-planetary nebula (PPN) and similar to other optically-thin shell-like PPNe such as IRAS 17436+5003 (Ueta et al. 2000; Gledhill et al. 2001).

Near-IR imaging polarimetry of HD 179821 (Gledhill et al. 2001) allowed the overlying stellar point-spread function (PSF) to be separated from the scattered light to provide an image of the dust shell in polarized flux in the inner 4 arcsec around the star. These images show a spatially-resolved ring of scattered light encircling the star, with an inner radius of between 1.1 and 1.6 arcsec (the star is not at the centre of the shell), indicating that both the near-IR and mid-IR emission arise from the same body of dust illuminated and heated by the star. By subtracting the stellar PSF, an image of the shell surface brightness in the near-IR, and hence the intrinsic shell polarization, can be formed. In this paper we use these quantities, along with the distribution of polarized

★E-mail: T.Gledhill@star.herts.ac.uk

flux, to fit scattering models to the observations in order to deduce the nebula geometry, dust distribution and the properties of the dust grains.

2 OBSERVATIONAL CONSTRAINTS

2.1 Imaging polarimetry observations

A *J*-band image of HD 179821 in polarized flux, obtained at the 3.8-m UK Infrared Telescope (UKIRT), is shown in Fig. 1. The polarimetric observations were made with the IRCAM infrared detector and the IRPOL polarization module and are described by Gledhill et al. (2001). A 2× warm magnifier gave a pixel scale of 0.143 arcsec. Fig. 1 clearly shows the scattered light to lie in a shell or ring surrounding the star. A circle of radius 1.9 arcsec is drawn on the image to indicate the peak intensity (in polarized flux) in the shell. Although there is evidence for structure in the scattered light, to a good approximation the shell is symmetric, with equal amounts of flux lying inside and outside the circle. The centre of symmetry (+), is offset from the stellar centroid (*) which lies 0.3 arcsec to the north, indicating that the star does not lie at the centre of the shell. Jura & Werner (1999) noted this offset in their 11.7 μm images, which shows that the thermal emission is also distributed in a shell around the star, as first observed by Hawkins et al. (1995). The bright shell seen in polarized flux is surrounded by a fainter halo of scattered light, which can be seen in our images out to a radius of approximately 5 arcsec from the star. In addition, Fig. 1 shows that polarized flux is recorded inside the bright shell. The brightness of HD 179821 in the near-IR ($K = 4.59 \pm 0.05$, Kastner & Weintraub 1995) means that alignment and subtraction residuals dominate the central region of our images, so that we have not been able to measure polarization closer than 1 arcsec to the star.

We take advantage of the radial symmetry to form azimuthally-averaged radial profiles of polarized flux and percentage polarization, shown in Fig. 2. The profiles are centred on the + symbol in Fig. 1. Since the observations were made through varying degrees of cloud cover, it has not been possible to calibrate the flux scale. The peak in polarized flux occurs at a radius of 1.9 arcsec at *J* and 2.0 arcsec at *K*. Given that the pixel scale is 0.14 arcsec and that the seeing conditions at the time were variable, the difference is not significant. The percentage polarization has peaks at 18.5 at *J* and 18.0 at *K*, both at a radius of 2.7 arcsec. In fact, the radial profiles in both polarized flux and percentage polarization are the same, within errors, at *J* and *K*. This suggests that the scattering properties of the dust are remarkably wavelength independent.

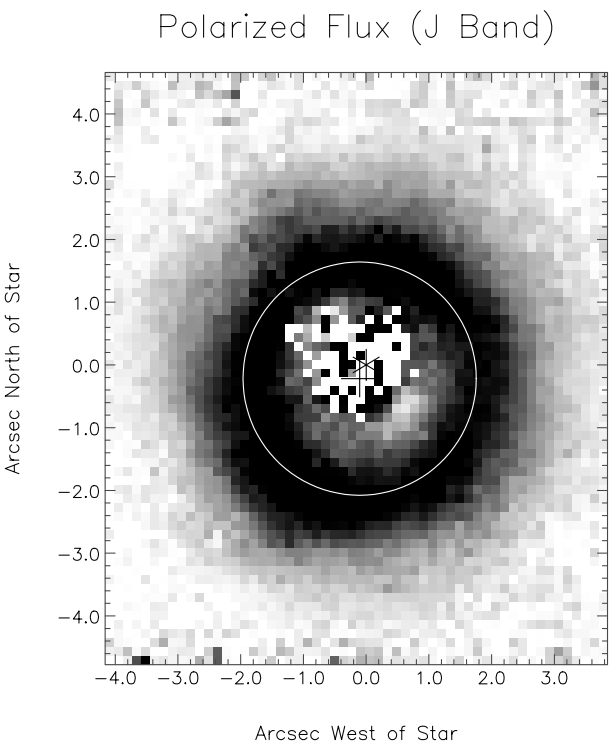

Figure 1. A *J*-band image in polarized flux of HD 179821 (IRAS 19114+0002). The data are from Gledhill et al. (2001). A circle of radius 1.9 arcsec, passing through the regions of peak flux, illustrates the symmetry of the shell. The centre of the circle is denoted by +, which is offset from the stellar centroid, denoted by *.

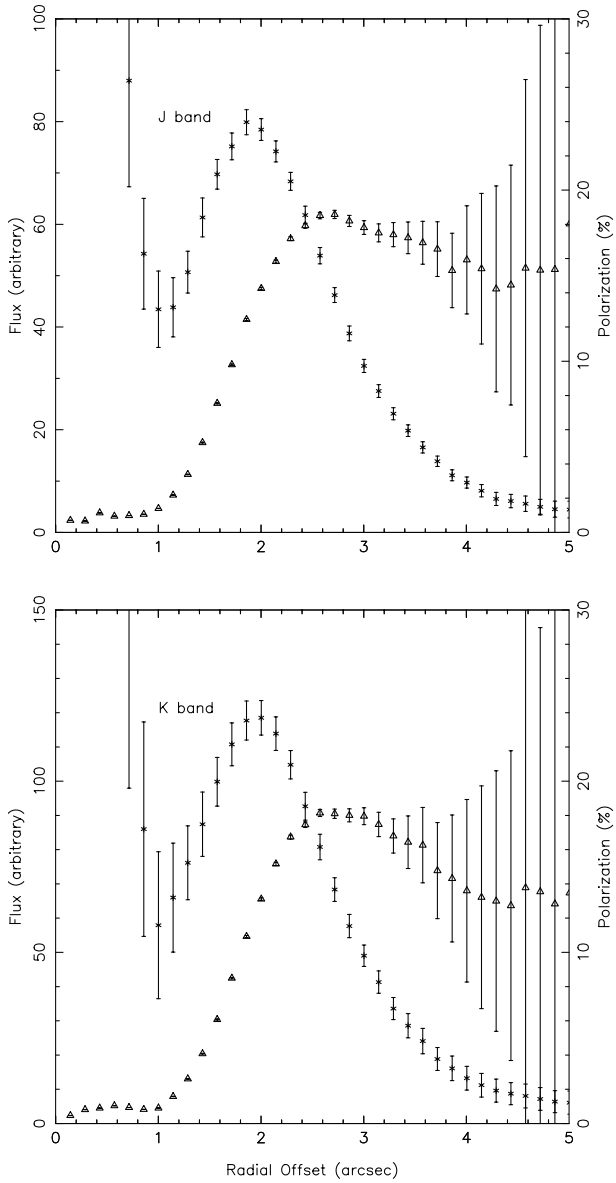

Figure 2. Azimuthally averaged radial profiles through the shell in the *J* (upper) and *K* (lower) wavebands. Polarized-flux measurements are shown as crosses and are plotted on an arbitrary flux scale. Percentage polarization is plotted as triangles according to the scale on the right.

2.2 PSF subtraction

The polarizations plotted in Fig. 2 were obtained by dividing the polarized flux (Fig. 1) by the total flux image. However, this includes a contribution from the unpolarized point-spread function (PSF) of the star, whose wings extend to cover the whole of our image. These polarizations are, therefore, *lower limits* on the intrinsic polarization of the shell, $P_{\rm int}$. To estimate the intrinsic polarization, we must subtract the PSF of the star to obtain an image of the shell in total flux so that

$$P_{\rm int} = \frac{\sqrt{Q^2 + U^2}}{I - I_{\rm psf}}, \qquad (1)$$

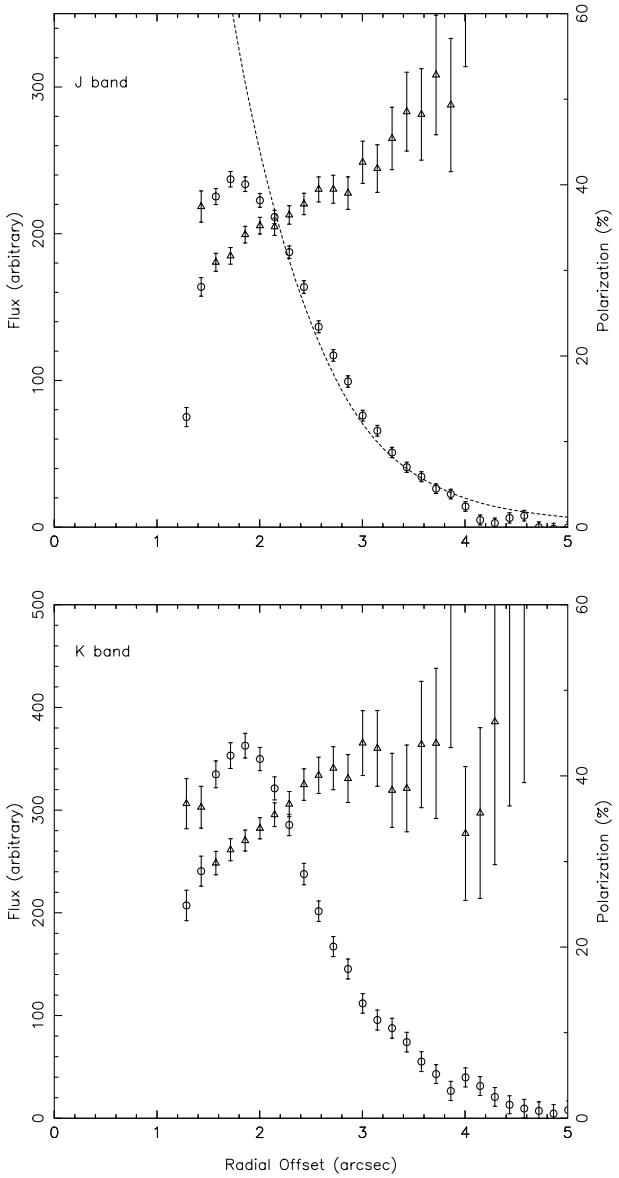

Figure 3. Azimuthally averaged radial profiles through the shell in the *J* (upper) and *K* (lower) wavebands, after subtraction of the stellar PSF. Total-flux measurements are shown as circles and are plotted on an arbitrary scale. Percentage polarization is plotted as triangles according to the scale on the right. At radii less than 1 arcsec, the total flux becomes negative indicating that the PSF has been over-subtracted in the central regions and consequently the turn-over in total flux at 1.8 arcsec radius may be an artifact. The dashed curve on the upper plot is *V*-band *HST* data (see text).

where I, Q and U are the Stokes intensities in the unsubtracted data and $I_{\rm psf}$ is the subtracted PSF flux. Note that the polarization angles (and hence the centro-symmetric scattering pattern) depend only on Q and U and are not affected by the PSF subtraction.

To perform the PSF subtraction we used scaled and aligned images of nearby bright stars: HD 178744 (B5V, $V = 6.3$) for the *J* band and HD 179626 (F7V, $V = 9.1$) for *K* band. Both stars were observed in the same polarimetric mode as the target for a total of 60 s each, resulting in a signal-to-noise ratio (SNR) in the wings of the PSF of greater than 2 out to a radius of 4 arcsec. The scaling was based on the peak pixel values of the stars. The PSF subtraction can only be approximate; seeing conditions at the time were variable and no better than $\sim$1 arcsec FWHM. Indeed, in all of our subtractions we found that the central pixel was surrounded by a negative 'hole' indicating over-subtraction. This suggests that either (i) the alignment between the target and PSF star could not be achieved to sufficient accuracy to correct the central bright regions or (ii) the shape of the PSF star was slightly different in the central peak (broader) compared with the target. Both could be due to slight variations in seeing. A reduction in the subtracted flux of 10 per cent was sufficient to turn the negative hole into a positive pedestal, so that the central flux is then under-subtracted. Subtraction of the PSF approximately doubles the polarization in the shell in both wavebands to between 30 and 40 per cent, so an error in the PSF subtraction of ± 10 per cent represents an error of ± 5 per cent in the intrinsic polarization. The fact that the polarization is observed to double indicates that although the SNR in the wings of the standard star is low compared with the target, there is sufficient signal to correct for the stellar PSF.

After subtraction of the PSF, radial profiles were formed of the total flux in the shell and of the intrinsic percentage polarization and these are shown in Fig. 3. The polarization now rises with increasing offset from the star, suggesting that the depolarizing effect of the stellar PSF increases with radius. As with the polarized flux, the profiles of total flux and percentage polarization show little variation between *J* and *K*. The error bars shown in Fig. 3 are derived from the spread in pixel values during the azimuthal averaging process and do not include any systematic errors that may arise from the PSF subtraction (above). In Fig. 3 we also plot the profile from the *V*-band *HST* image of Ueta et al. (2000),[1] which we have obtained by smoothing their image to the 0.9 arcsec FWHM seeing of our UKIRT data, forming the azimuthally-averaged profile and then scaling it to our intensity profile at a radial offset of 1.9 arcsec. Although the *HST* image has not been corrected for the WFPC2 PSF, its contribution to the shell brightness at several arcsec offset from the star will be much less than in our ground-based data. The similarity of the *HST* and PSF-subtracted UKIRT profiles gives us confidence that our PSF subtraction is fairly sound. Indeed, both profiles approximate an r^{-3} surface brightness dependence, as expected for optically-thin scattering in a shell with an r^{-2} density fall-off. At a radial offset of less that 1.5 arcsec, the PSF-corrected flux shown in Fig. 3 starts to decrease, and at radii of less than 1.0 arcsec, it becomes negative. This indicates an over-subtraction in the central regions. There is no indication from the *HST* data of a decrease in shell brightness in the central regions, and so this may be an artifact of the PSF subtraction. It is also possible that too much flux has been subtracted at radii > 1.5 arcsec and that the intrinsic polarization is lower than we have estimated. To try to corroborate the PSF subtraction further, we also used a separate *J*-band observation of

[1] Courtesy of the NCSA Astronomy Digital Image Library (ADIL).

HD 179821 and PSF standard, taken in 1999 June (a year after the polarimetry observations) to form a PSF-subtracted image of the shell. We then divided this image into our (1998 May) polarized-flux image and find that the shell polarization is the same, within errors, as that shown in Fig. 3.

2.3 Shell properties

2.3.1 Relative brightness and colour

A measure of the scattering cross-section, C_{sca}, of the dust in the shell is provided by the ratio of the shell surface brightness to the brightness of the star. This ratio, which we call S, is intrinsic to the shell and independent of interstellar extinction. The variation of S with wavelength provides a strong diagnostic of the dust model, in particular the size distribution. To quantify the surface brightness of the shell, we use the PSF-subtracted azimuthally-averaged radial profile (Fig. 3) and take the counts in a bin at a radial offset of 2.2 arcsec. The ratio of this value to the counts in an equivalent bin at the position of the star in the *unsubtracted* data gives an estimate of S, the relative brightness of the shell. Note that the brightness of the shell at the position of the star is negligible compared with that of the star itself. We also estimate S for the 0.55 μm WFPC2 observations of Ueta et al. (2000) shown in Fig. 3. Since this data is not PSF subtracted, $S_{0.55}$ is likely to be an upper limit on the shell brightness in the V band. We summarize these quantities, along with the wavelength variation, in Table 1. As can be seen, there is remarkably little variation in the relative shell brightness, and hence the scattering efficiency, between J and K. The ratio $S_J/S_K = 1.32$ is much less than the λ^{-4} dependence expected for scattering from small (Rayleigh) particles and gives a colour excess for the shell of $E(J-K) = -0.3$. This 'grey' scattering law was also noted by Kastner & Weintraub (1995), who suggested that the grains must be large and/or have unusual scattering properties.

Table 1. Shell parameters, derived from the PSF-subtracted observations, in each waveband. P_λ is the percentage polarization at a radial offset of 1.9 arcsec from the centre of the shell. S_λ is a measure of the shell brightness relative to the star. The errors on S_J and S_K assume a 10 per cent error in the PSF subtraction. The error on $S_{0.55}$ (from which a PSF has not been subtracted) is based on photon noise.

	0.55 μm	J	K
P_λ	–	34.2 ± 0.9	32.5 ± 1.3
$S_\lambda \times 10^2$	1.49 ± 0.09	0.63 ± 0.06	0.47 ± 0.05
S_λ/S_K	$<3.15 \pm 0.36$	1.32 ± 0.19	1.00

2.3.2 Extinction

An estimate of the extinction to the star can be made based on the expected colour for a star of spectral type G5 Ia and the observed fluxes (HKV89); however, there is disagreement over the exact stellar temperature. Hawkins et al. (1995) found $E(B-V) = 0.6$, based on a photospheric temperature of $T_{eff} = 5100$ K, which, assuming a standard interstellar reddening law, leads to $A_v = 1.8$ mag. Reddy & Hrivnak (1999) derive a higher temperature of $T_{eff} = 6750$ K based on an analysis of the optical spectrum. The implied bluer intrinsic colour leads to a higher estimate of $A_v = 4.0$ mag. However, in a further spectral analysis, Thévenin et al. (2000) dispute this higher temperature and derive $T_{eff} = 5660 \pm 70$ K. This lower temperature gives a colour excess of $E(B-V) = 0.9$ and, again assuming a standard interstellar reddening law, an extinction of $A_v = 2.9$ mag. At a distance of 6 kpc, a significant fraction of this extinction must be interstellar, and HKV89 quote 2.0 mag for the interstellar component 'assuming a distance of a few kpc'. We adopt the constraint that the intrinsic extinction, caused by the circumstellar shell, should be less than 2 mag in the V band.

2.3.3 Chemistry

HD 179821 is an O-rich star with O/C = 2.6 (Reddy & Hrivnak 1999). The envelope chemistry is also O-rich with OH masers detected with the same velocity range as the CO emission (Likkel 1989; Likkel et al. 1991) and lying in a shell of similar extent to the dust shell (Claussen 1993). A weak feature at 10 μm in the IRAS LRS spectrum (HKV89) indicates the presence of silicate grains. More recent *ISO* results suggest that the dust is composed mainly of a mixture of amorphous and crystalline silicates (Waters et al. 1996).

3 SCATTERING MODELS

3.1 Modelling procedure

Details of the Monte Carlo modelling procedure are given in Appendix A. To compare the model results with the observations, the model images are convolved with a Gaussian profile of FWHM 0.9 arcsec, simulating the seeing at the time of the observations. They are then processed in the same way as the observations, by forming azimuthally-averaged radial profiles. This also takes

Table 2. A summary of parameters for each model. Numbers in parentheses are powers of 10. The AS1 dust models are 'astronomical silicate' with $a_{min} = 0.05$ μm, $a_{max} = 2.0$ μm and $\beta = 6.0$. The AS2 dust model has $\beta = 5.5$. α, ϵ, γ are parameters of the dust distribution (Section 3.3), r_{in} is the inner radius of the dust shell in metres and N_{in} the grain number density at that point in m^{-3}. $S_{1.2}/S_{2.2}$ is the ratio of the relative shell brightness at $\lambda = 1.2$ μm and $\lambda = 2.2$ μm and a measure of the colour of the shell. $\tau_{1.2}$ and $\tau_{2.2}$ are the optical depths through the shell to the star. For the equatorially enhanced models, values along both pole and equator (pole/equator) are given. M_d is the mass of dust in the shell in units of $M_\odot$. The distance, D, is assumed to be 6 kpc.

Model	Dust	α	ϵ	γ	r_{in}	N_{in}	$S_{1.2}S_{2.2}$	$\tau_{1.2}$	$\tau_{2.2}$	M_d
S1	AS1	−2.0	0.0	0.0	1.44(15)	2.70(−1)	5.58	2.57(−1)	7.70(−3)	8.20(−2)
D1	AS2	−2.0	0.0	0.0	1.44(15)	1.40(−1)	4.26	2.27(−1)	6.68(−2)	5.10(−2)
D2	AS2	−2.0	1.0	10.0	1.44(15)	1.14(−1)	4.22	1.85(−1)/3.69(−1)	5.44(−2)/1.09(−1)	5.70(−2)
D3	AS2	−2.0	2.0	3.0	1.44(15)	7.50(−2)	4.10	1.22(−1)/3.64(−1)	3.58(−2)/1.07(−1)	5.90(−2)
D4	AS2	−2.0	9.0	3.0	1.44(15)	2.90(−2)	3.93	4.70(−2)/4.70(−1)	1.38(−2)/1.38(−1)	6.60(−2)
D5	AS2	−2.0	9.0	10.0	1.44(15)	4.60(−2)	4.09	7.45(−2)/7.44(−1)	2.19(−2)/2.19(−1)	7.20(−2)

advantage of the symmetry in the model to increase the signal to noise of the computations for a given number of model photons. The model profiles are normalized to the observations using the observed polarized-flux peak at 1.9 arcsec, since this is not subject to PSF subtraction errors. We calculate the ratio of the shell brightness to that of the star for each model and normalize this to the observations (S_λ in Table 1) by varying the dust-grain number density, $N_{\rm in}$. This provides a determination of $N_{\rm in}$ independent of flux calibration, foreground extinction or knowledge of the spectrum of the star. By assuming a distance, D, to the object, the physical parameters of the model such as optical depth, τ, and dust mass, $M_{\rm d}$, shown in Table 2 are obtained.

3.2 Spherically-symmetric models

To simulate a spherically-symmetric shell we use a dust density of the form

$$N(r) = N_{\rm in}(r/r_{\rm in})^{-\alpha} \qquad (2)$$

with $\alpha = 2$, corresponding to a constant mass-loss rate throughout

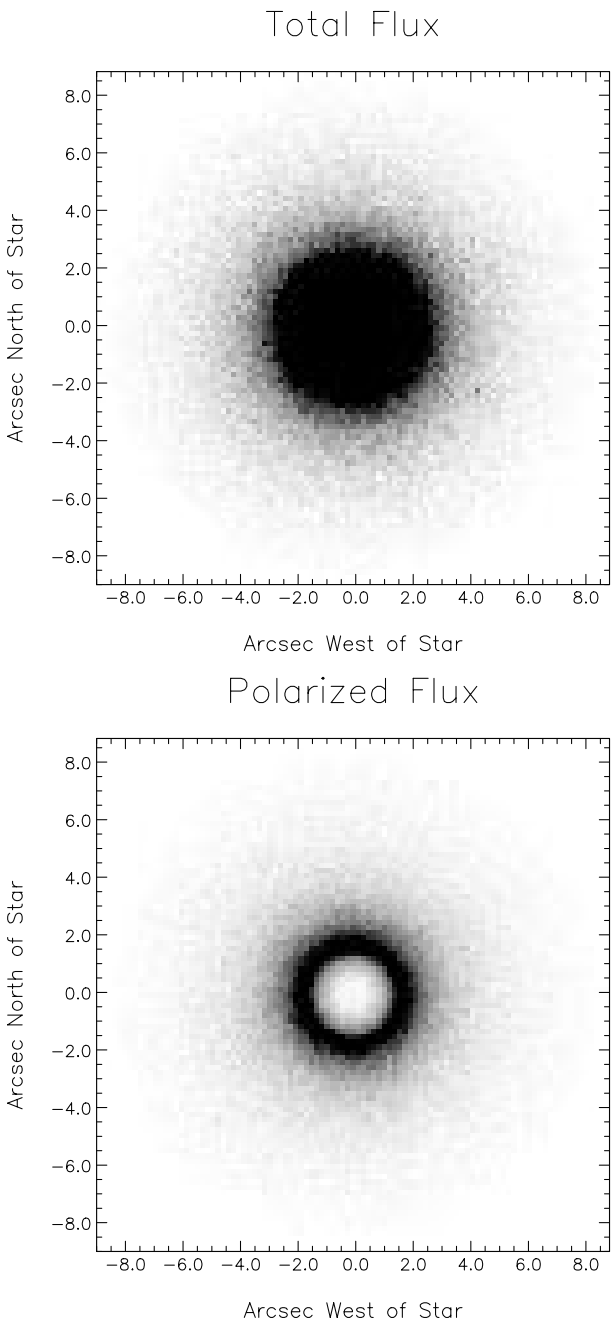

Figure 4. A spherical-shell-scattering model (S1) showing the distribution of total and polarized flux at 1.2 μm. The images have not been smoothed to match the observational data and so retain a spatial resolution of 0.18 arcsec. The direct light from the star occupies a single pixel at the centre of the image and has a total flux count of 764 000 (in arbitrary units). The images are scaled between 0 (white) and 50 (black) in the same (arbitrary) units.

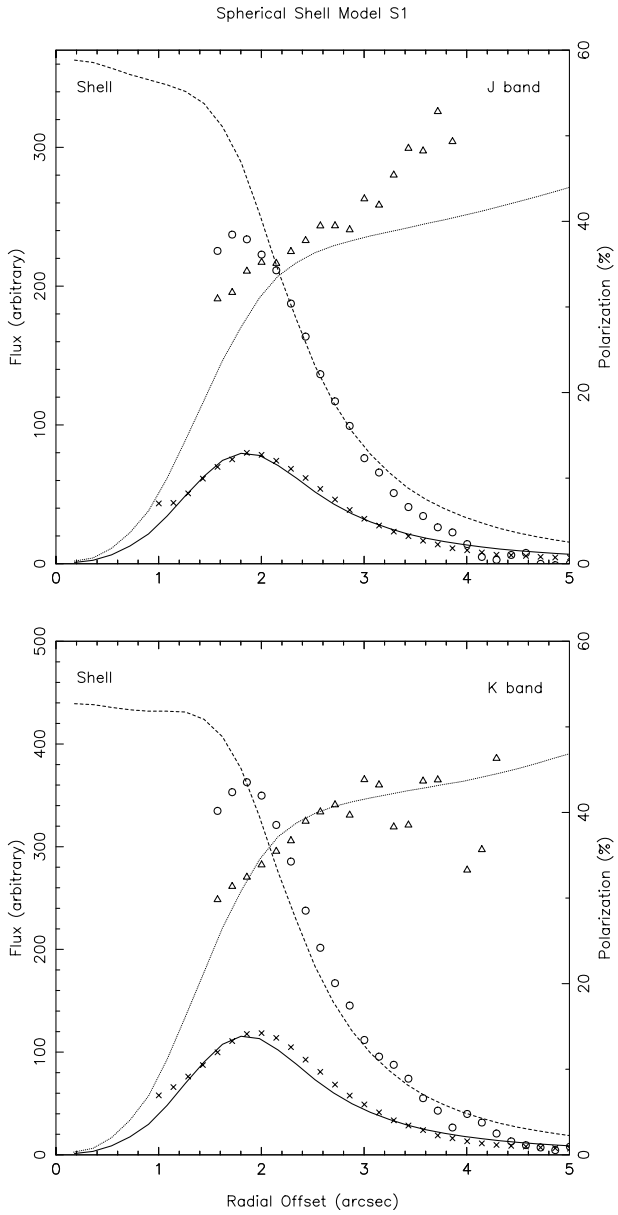

Figure 5. A comparison of azimuthally-averaged radial profiles through the spherical-shell model S1 with those through the data (Figs 2 and 3). The error bars, and data points in the central region, have been omitted for clarity. The model profiles are scaled to the observations by normalizing the model polarized flux (solid line) to the observed polarized flux (×) at a radius of 1.9 arcsec. This also determines the scaling on the total-flux curves (dashed lines). Percentage polarization is shown as a dotted line.

the history of the shell. In view of the O-rich chemistry we initially assume a population of bare silicate grains. We treat as free parameters the inner radius of the shell, $r_{\rm in}$, the dust-grain number density at this radius, $N_{\rm in}$ and the grain size distribution parameter β (see Appendix A). In order to generate the observed degrees of polarization of 30 to 40 per cent after scattering in a realistic geometry such as a shell, the grains themselves must be able to produce 70 to 80 per cent polarization. This requires small grains so we initially set $\beta = 6.0$ (AS1, Table 2).

A scattering model using the spherical-shell geometry and the AS1 grain model is shown in Fig. 4. The ring structure, seen in polarized flux in the observations (Fig. 1), is clearly seen in the model polarized-flux image, but not in the total flux image. This is because, for lines of sight (LOS) that pass through the inner hollow region of the shell, scattering occurs predominantly from dust in front of the star and, therefore, through forward-throwing angles. For these angles, there is a large contribution to total flux but little to the polarized flux (which is zero for a LOS through the star). The effect is to 'fill in' the central region of the shell in total flux but to leave a 'hole' in polarized flux. For a spherically-symmetric detached shell, the detached nature of the shell, with a clear boundary at the inner radius $r_{\rm in}$, will only be evident observationally (in scattered light) in a polarized-flux image.

The model profiles are shown in comparison with the observed profiles in Fig. 5. The observed profiles are plotted using the same symbols as in Figs 2 and 3 but with the error bars omitted for clarity. Model calculations at 1.2 and 2.2 μm are compared with *J*- and *K*-band observations, respectively. The characteristics of the model are summarized in Table 2. We find that the S1 model simulates the observations quite well, suggesting that a spherical shell is a good approximation to the actual geometry of the CSE. The shape of the polarized-flux profile and the position of its peak depend on the scattering-asymmetry parameter, g (see Appendix B), and the radius of the inner edge of the shell, $r_{\rm in}$. For the S1 model, $g = 0.34$ at 1.2 μm (Table B2). If g becomes too large (the grains are too forward-throwing in their scattering) then the polarized-flux peak moves closer to the star, as the dust in front of the star begins to dominate the scattering. We find that, in order to fit the observed polarized-flux profile, the dust around HD 179821 must have $g < 0.6$.

To produce the high degrees of observed polarization we have had to use a size distribution with a steep power law ($\beta = 6$) so that a large proportion of small (highly-polarizing) grains are included in the distribution. This produces far too much wavelength dependence in the model and consequently the shell is much too faint relative to the star at the longer wavelength ($S_{1.2}/S_{2.2} = 5.8$ in Table 2). This suggests that we must construct a model that can produce high polarization from larger (greyer) particles. One possibility is to move to an axisymmetric dust distribution.

3.3 Equatorially enhanced models

The spherically-symmetric geometry results in long lines of sight through the shell which sample a wide range of scattering angles. Since maximum polarization is only produced for scattering angles around 90° the geometry acts to reduce the maximum polarization of the AS1 dust model from ~80 to ~40 per cent. By concentrating the dust in the plane of the sky, scattering angles around 90° are given more weight and the polarization can be increased. This can be achieved using a model with an equatorial density enhancement which is then viewed pole-on. To simulate this we use a dust density of the form

$$N(r) = N_{\rm in}(r/r_{\rm in})^{-\alpha}(1 + \epsilon \sin^{\gamma}\theta), \qquad (3)$$

which is similar to that used to generate axisymmetry in models of planetary nebulae (e.g. Kahn & West 1985; Kwok 2000). The radial density fall-off is now modified to create a density enhancement of $1 + \epsilon$ between the equator and pole. The parameter γ controls the way density increases with polar angle, θ, with higher values of γ concentrating more material in the equatorial region.

In Fig. 6 we show plots of the radial dependence of surface brightness and polarization at 1.2 μm for five 'disc' models with various values of ϵ and γ. These models, D1 to D5, simulate

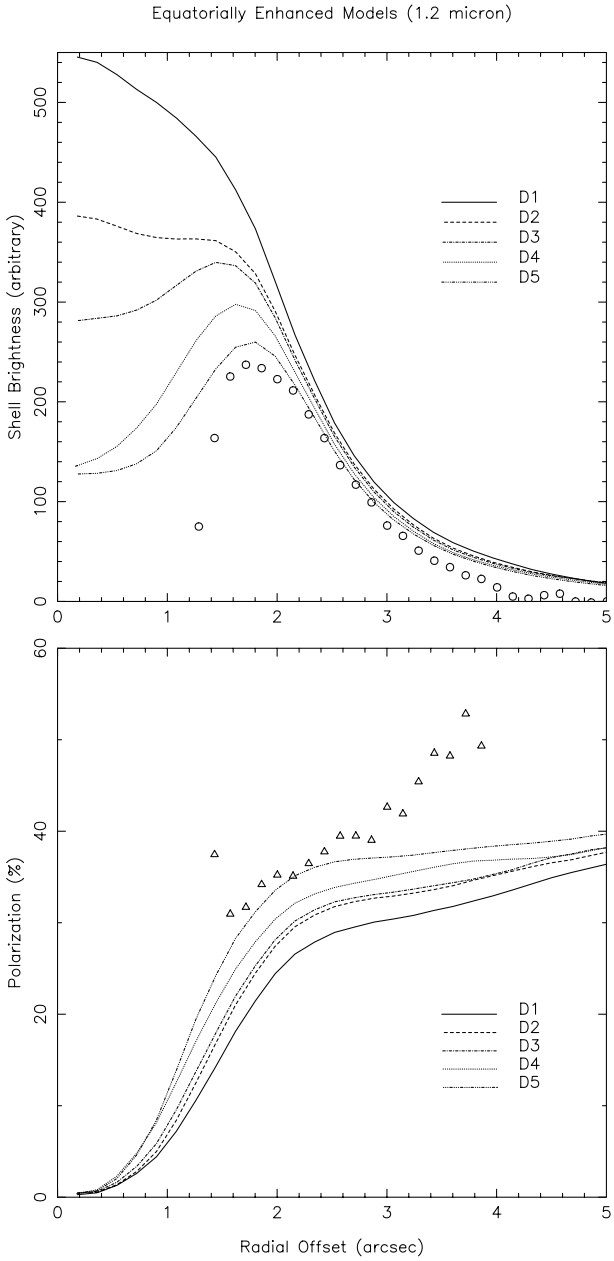

Figure 6. Azimuthally averaged radial profiles through shell models with equatorially enhanced dust distributions, compared with the data (Fig. 3). The error bars on the data points have been omitted for clarity. Profiles of both total flux (upper panel) and percentage polarization (lower panel) are shown. The parameters for the models are listed in Table 2.

increasing concentrations of dust in the equatorial plane, with D1 being a spherically-symmetric model and D5 being the most flattened with a density contrast (equator to pole) of 10:1 and an angular dependence of $\sin^{10}\theta$. All are viewed pole-on and have $\alpha = 2$ with the inner radius, $r_{\rm in}$, fixed at 1.44×10^{15} m ($D = 6$ kpc). A silicate-dust model, AS2, is used that differs from the AS1 model used in Section 3.2 in that it has a slightly shallower power law for the size distribution with $\beta = 5.5$, thus including larger grains.

Only the D5 model with a 10:1 density contrast ($\epsilon = 10$, $\gamma = 10$) approaches the observed polarization. However, increasing the density contrast this much also acts to flatten the polarization profile so that it no longer matches the observed rise in polarization with radial offset. Increasing the density contrast between equator and poles also causes the intensity profile to turn over at small radial offsets until, for the D5 model, there is a peak in intensity similar to that observed in polarized flux. In other words, there is now a central 'hole' in intensity as well as polarized flux (Fig. 1). There is no evidence for such a hole or inner-shell boundary in the *V*-band *HST* images (Ueta et al. 2000), although running the D5 simulation at 0.55 μm also produces a central hole. This indicates that any density enhancement must be slight (D1 and D2 models).

It is also apparent from Table 2 that concentrating the dust in the equatorial plane does nothing to solve the colour problem – the shell is still too blue. The $S_{1.2}/S_{2.2}$ index does decrease slightly for the more axisymmetric models but this is due to an increase in extinction for paths in the equatorial plane. Changes to the geometry alone cannot increase the polarization produced by the dust models based on astronomical silicate so as to match simultaneously the observed polarization and still retain colour neutral scattering at *J* and *K*.

4 DISCUSSION

The results of the previous section indicate that the radial distribution of polarized flux, surface brightness and percentage polarization in the near-IR can be modelled using a spherical distribution of dust with a sharp inner boundary and an r^{-2} density fall-off. It has not been possible simultaneously to fit the degree of polarization and the low colour excess ($E(J-K) = -0.3$), since all of the models considered produce scattering that is far too blue. The shell could easily be reddened by increasing the optical depth; however, this would also reduce the polarization. In addition, examination of the *V*-band *HST* image of Ueta et al. (2000) suggests that the shell is optically thin in the *V* band, since the surface brightness profile (Fig. 3) is very similar to that of our *J*-band data.

So far our dust model has been based on 'astronomical silicate' (Draine 1995), which has been widely used to model reflection nebulae in star-formation regions. However, silicates only produce high degrees of polarization for small grains (close to the Rayleigh limit), which inevitably exhibit strong colour effects in the scattered intensities, producing predominantly 'blue' reflection nebulae. In Appendix B we tabulate the scattering properties of various size distributions of 'astronomical silicate' and other materials. For an optically-thin nebula (where absorption is not important), the ratio of scattering cross-sections at 1.2 and 2.2 μm gives a reliable indication of the nebula colour. In order to produce a nebula with a ratio of scattering cross-sections $C_{\rm sca}(1.2\,\mu{\rm m})/C_{\rm sca}(2.2\,\mu{\rm m}) < 2.0$, a power-law size distribution of astronomical silicates with $a_{\rm min} = 0.05\,\mu$m and $a_{\rm max} = 2.0\,\mu$m must have an index $\beta < 4.0$. Such a distribution produces very little polarization and cannot fit our observations. The same is true of the other forms of silicate listed (olivine, pyroxene), which have similar refractive indices in the near-IR. As mentioned in Section 2.2, the PSF subtraction is only approximate, so that it is possible we have over-estimated the intrinsic shell polarization, in which case some of the more highly-polarizing grain models (Table B2) may account for the observations. However, even if we take the raw (before PSF subtraction) polarization of 20 per cent at *J* and *K* as the intrinsic polarization of the shell, a bare silicate-dust model cannot produce the required colours. We therefore rule out scattering from spherical silicate particles as the dominant polarizing mechanism.

4.1 Dust composition

Some of the emission features seen towards HD 179821 may be due to metal oxides in the shell, such as magnesium-iron-oxides (Ueta et al. 2001). There is evidence that these materials may contribute to the observed structure in the 15–24 μm spectral region (Henning et al. 1995; Waters et al. 1996). We have calculated the scattering properties for $Fe_{0.4}Mg_{0.6}O$ (Henning et al. 1995) and find that this material produces more polarization than silicates, for an equivalent size distribution. A scattering-cross-section ratio of $R_{1.2/2.2} < 2.0$ can be produced for a power-law size index of $\beta < 4.5$ (Table B2), which results in a maximum polarization of < 60 per cent at 1.2 μm and < 50 per cent at 2.2 μm. This is still not sufficient to fit the observed shell polarization, although it could account for the ∼20 per cent polarization observed in the raw (non-PSF-corrected) data. The material does produce around 10 per cent more polarization at 1.2 μm than at 2.2 μm, though, which is contrary to our *J*- and *K*-band observations. In addition, even if metal oxides are present in the shell, it is not clear that they would be majority contributors to the scattered light or that they would be distributed so evenly.

The *ISO* spectra of HD 179821 also show evidence for crystalline ice in the form of a 43 μm 'bump', along with various features attributable to forms of crystalline silicates (Waters et al. 1996). We have calculated the scattering properties for ice-coated silicates with a coating thickness equal to the grain radius (Table B2). Ices, especially water ice with a low refractive index, are highly polarizing so that a coating of ice can increase the polarization of a silicate grain core significantly (by an amount increasing with the coating thickness). However, the scattering properties of the ice are more wavelength sensitive than silicates, so that there is a trade-off between increasing the maximum polarization of the dust by applying an ice coating and maintaining a grey scattering efficiency. Again we have not been able to produce the required high polarization and grey scattering using ice-coated silicates.

4.2 Particle size distribution

The power-law size distribution used in the previous section has upper and lower cut-offs on the grain size so as to keep the number of grains finite. We have adopted the values $a_{\rm min} = 0.05\,\mu$m and $a_{\rm max} = 2.0\,\mu$m, rather than treating them as free model parameters, and so we should examine these assumed values. For any size distribution, the particle sizes that contribute most to scattering will be those that maximize the weighted scattering cross-section, $N(a)C_{\rm sca}(a)$. In order to produce the high polarizations that we see in the *J*- and *K*-band observations, these particles must be small, typically with size parameter $x < 1$ (or radius $a < 0.2\,\mu$m at $\lambda = 1.2\,\mu$m), where $x = 2\pi a/\lambda$. This is illustrated in Fig. 7, which

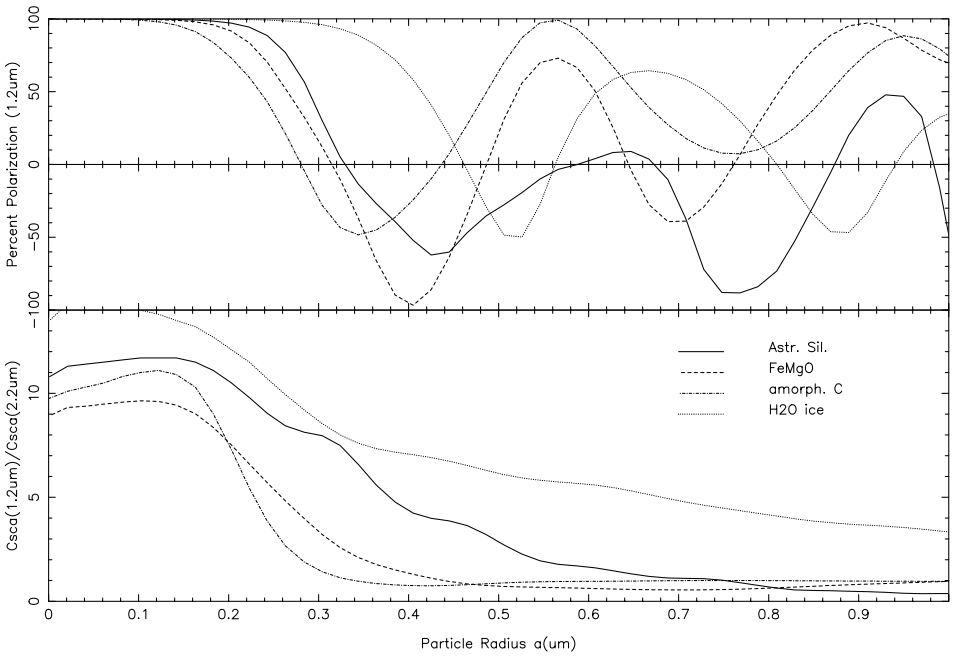

Figure 7. Linear polarization at $\lambda = 1.2\,\mu$m (top panel) and the ratio of scattering cross-sections at $\lambda = 1.2\,\mu$m and $\lambda = 2.2\,\mu$m (bottom panel) as a function of grain radius, a, for various materials.

shows the polarization produced at $\lambda = 1.2\,\mu$m as a function of a. Particles larger than $x = 1$ produce less polarization and of varying sign (especially for the dielectric materials such as silicate), which sum to small values when a distribution of sizes is taken. Since the scattering cross-section increases with particle radius a as up to the sixth power, a steep power-law index β is required for the size distribution to ensure that the smaller (polarizing) particles are present in sufficient numbers to dominate the scattered light. This in turn means that the scattering properties are rather insensitive to the upper size cut-off $a_{\rm max}$, since there are too few particles of this size to contribute. At the small-size end of the distribution ($x < 1$), scattering is approaching the Rayleigh limit, where the cross-section falls off as $C_{\rm sca} \propto a^6$ and polarization is a maximum. As long as $a_{\rm min}$ is small enough to include Rayleigh particles, then reducing it further has very little effect on the polarization or colour of the scattered light. For values of $\beta < 6$, the smallest particles do not contribute to the scattered flux. Fig. 7 shows that it is not possible to generate the observed high polarization and neutral nebula colour by adjustments to the power-law size distribution, at least for the materials we have considered. The range of particle sizes responsible for producing high polarization and neutral colour – low $C_{\rm sca}(1.2\,\mu{\rm m})/C_{\rm sca}(2.2\,\mu{\rm m})$ – are mutually exclusive. This would also be the case for other size-distribution functions, such as a modified power-law (Jura 1994) or exponential distribution (Jura 1975).

4.3 Non-spherical or composite particles

It is well known that much of the dust in the Galaxy is composed of non-spherical grains that are responsible for phenomena such as the interstellar linear and circular polarization (Whittet 1995; Martin 1972). Mid-IR polarization observed in star-forming regions (e.g. OMC1, Aitken et al. 1997) shows that aligned, non-spherical particles are present in circumstellar environments also. Given the wide-spread distribution of non-spherical grains, it seems reasonable to assume that at least a proportion of the dust at its point of origin, in the circumstellar envelopes of evolved stars, will also be non-spherical.

The scattering properties of highly-spheroidal particles differ significantly from spheres and can show a combination of the characteristics of larger and smaller particles. Zakharova & Mishchenko (2000) find that for spheroids with aspect ratios of 20:1, the polarization reaches 100 per cent at a scattering angle of 90°, typical of Rayleigh scattering, even for particles with size parameters $x = 3.5$. However, the scattering efficiency as a function of size parameter is more typical of that of larger spheres, showing a weak dependence on x. It therefore seems plausible that the high polarizations and weak dependence of $C_{\rm sca}$ on grain size, required to explain our observations, may be satisfied if the scatterers are spheroidal with large aspect ratios (needle-like or plate-like). An alternative to highly elongated particles could be provided by composite or aggregate particles where the overall size of the particle is comparable with the wavelength, but many of the scattering properties (such as the polarization) are characteristic of the component sizes. Such behaviour has been seen in low-density aggregates of spheres (West 1991).

4.4 Dust mass, extinction and the distance to HD 179821

The dust optical depths shown in Table 2 have been obtained by fitting to the scattered surface brightness of the shell relative to the star, and are intrinsic to the object and not dependent on the assumed distance. If the object is closer than 6 kpc then path-lengths through the shell would decrease and the dust density would have to be increased to maintain the observed shell brightness (and hence optical depth). So our model fits do not directly constrain the distance estimates. Using the silicate-dust model and spherical (S1) geometry, we calculate an extinction to the star at 0.55 μm (roughly V band) of $\tau_{0.55} = 1.67$. This is consistent with estimates of the extinction to the star in the V band of between 1 and 2 mag (Section 2.3.3).

For the S1 model, we calculate a dust mass of $M_{\rm d} = 0.08\,{\rm M}_{\odot}$,

assuming an outer shell radius of 9 arcsec (Kastner & Weintraub 1995), a distance of 6 kpc and a density of 3.0×10^3 kg m^{-3} for silicate dust. This is of the same order as estimates of the dust mass obtained from mid-IR modelling of 0.03 $M_\odot$ (Jura & Werner 1999) and 0.04 $M_\odot$ (Hawkins et al. 1995). These authors assume values for the gas-to-dust mass ratio of between 100 and 160, which gives a total (gas + dust) mass in our model of between 8 and 13 $M_\odot$. Our estimate of M_d is sensitive to the dust model, in particular the scattering cross-section, and could easily be smaller, in agreement with the estimates from mid-IR emission. For example, increasing the scattering cross-section by using slightly larger grains (D1 in Table 2) gives $M_d = 0.05\,M_\odot$, although this no longer fits the observed polarizations.

5 CONCLUSIONS

The circumstellar envelope of the evolved star HD 179821 is seen by scattered light in the near-IR and appears as a detached shell in linearly-polarized light. We have used observations of a PSF-calibration star to subtract the atmospherically-scattered PSF of HD 179821 in order to obtain an image of the shell and hence calculate its intrinsic linear polarization. We find high degrees of polarization, between 30 and 40 per cent, in both *J* and *K* bands, with evidence for a gradual increase in polarization with radial offset from the star. The colours are remarkably neutral for scattering, with a colour excess in the shell of $E(J-K) = -0.3$.

We use an axisymmetric-scattering code to model the *J*- and *K*-band observations and find that the distribution of polarized and total flux can be produced by a spherically-symmetric shell of dust with an r^{-2} density distribution. The model shows that, when scattering from such a spherically-symmetric shell, the detached nature of the shell is only apparent in polarized flux, with the total flux image showing no evidence for an inner boundary. By fitting the models to the observed brightness of the shell relative to the star, we obtain an optical depth to the star at 1.2 μm of $\tau_{1.2} = 0.26$, which is consistent with estimates of the *V*-band extinction. Assuming a distance to HD 179821 of 6 kpc, we derive an inner-shell radius of $r_{in} = 1.44 \times 10^{15}$ m, a dust number density of $N_{in} = 2.70 \times 10^{-1}$ m^{-3} at r_{in} and a total mass of dust in the shell of $M_d = 0.08\,M_\odot$, assuming a power-law size distribution of silicate grains. These estimates are sensitive to uncertainties in the dust model but the dust mass is of the same order as that derived from mid-IR imaging of the warm dust.

We have experimented with equatorially enhanced density distributions, viewed pole-on, but conclude that if the shell does have an increased concentration of dust in the equatorial plane then the contrast between equator and poles cannot be much more than 2:1, otherwise the radial dependence of linear polarization becomes too flat to fit the observations.

Although the spherical-shell model fits the observed distributions of total and polarized flux quite well, we have not been able to account simultaneously for the high degrees of linear polarization and the unusually 'grey' scattering at *J* and *K*. We attribute this to inadequacies in the dust model and have explored various materials such as silicates, carbons, metal oxide and also ice-coated particles. If the high intrinsic polarizations implied by our PSF subtraction are correct, then none of the materials has reproduced the observed colours and polarizations and a distribution of homogeneous spherical particles, as assumed here, is unlikely to do so. Instead, we suggest that the dust surrounding HD 179821 may consist of either highly elongated needle- or plate-like particles or of composite grains with many smaller inclusions.

It would be very useful to obtain higher spatial resolution imaging polarimetry observations (such as coronographic 8-m data) and/or spectropolarimetry over the optical and near-IR, to ascertain the polarization in the shell more accurately and to determine the scattering behaviour of the dust over a wider wavelength range.

ACKNOWLEDGMENTS

We are grateful to François Ménard for allowing us to use and modify his original Monte Carlo scattering code. Phil Lucas is thanked for assistance with scattering from coated spheres. We thank the NSCA Astronomy Digital Image Library (ADIL). Use was made of the SIMBAD astronomical data base. The modelling in this paper was based on data taken at the United Kingdom Infrared Telescope. An anonymous referee is thanked for helpful comments.

REFERENCES

Aitken D. K., Smith C. H., Moore T. J. T., Roche P. F., Fujiyoshi T., Wright C. M., 1997, MNRAS, 286, 85
Bohren C. F., Huffman D. R., 1983, Absorption and Scattering of Light by Small Particles. Wiley, New York
Claussen M. J., 1993, in Clegg A. W., Nedoluha G. E., eds, Astrophysical Masers. Springer, Berlin, p. 353
Dorschner J., Begemann B., Henning Th., Jäger C., Mutschke H., 1995, A&A, 300, 503
Draine B. T., 1985, ApJS, 57, 587
Gledhill T. M., Chrysostomou A., Hough J. H., Yates J. A., 2001, MNRAS, 322, 321
Hawkins G. W., Skinner C. J., Meixner M. M., Jernigan J. G., Arens J. F., Keto E., Graham J. R., 1995, ApJ, 452, 314
Henning Th., Begemann B., Mutschke H., Dorschner J., 1995, A&AS, 112, 143
Hrivnak B. J., Kwok S., Volk K. M., 1989, ApJ, 346, 265 (HKV89)
Jura M., 1975, AJ, 89, 277
Jura M., 1994, ApJ, 434, 713
Jura M., Werner M. W., 1999, ApJ, 525, L113
Kahn F. D., West K. A., 1985, MNRAS, 212, 837
Kastner J. H., Weintraub D. A., 1995, ApJ, 452, 833
Kwok S., 2000, The Origin and Evolution of Planetary Nebulae, Cambridge Astrophysics Series 31. Cambridge Univ. Press
Likkel L., 1989, ApJ, 344, 350
Likkel L., Forveille T., Omont A., Morris M., 1991, A&A, 246, 153
Martin P. G., 1972, MNRAS, 159, 179
Ménard F., 1989, PhD thesis, Univ. Montreal
Preibisch Th., Ossenkopf V., Yorke H. W., Henning Th., 1993, A&A, 279, 577
Reddy B. E., Hrivnak B. J., 1999, AJ, 117, 1834
Thévenin F., Parthasarathy M., Jasniewicz G., 2000, A&A, 359, 138
Ueta T., Meixner M., Bobrowsky M., 2000, ApJ, 528, 861
Ueta T., Speck A. K., Meixner M., Dayal A., Hora J. L., Fazio G., Deutsch L. K., Hoffmann W. F., 2001, in Szczerba R., Tylenda R., Gorny S. K., eds, Astrophysics and Space Science Library, Vol. 265, Post-AGB Objects as a Phase of Stellar Evolution. p. 339
Warren S. G., 1984, Appl. Opt., 23, 1206
Waters L. B. F. M., Molster F. J., de Jong T., Beintema D. A. et al., 1996, A&A, 315, L361
West R. A., 1991, Appl. Opt., 30, 5316
Whittet D. C. B., 1995, in Greenberg J. M., ed., The Cosmic Dust Connection. Kluwer, Dordrecht, p. 155
Zakharova N. T., Mishchenko M. I., 2000, Appl. Opt., 39, 5052

APPENDIX A: DETAILS OF THE MONTE CARLO SCATTERING MODEL

The scattering models are computed using a modified version of the Monte Carlo scattering code of Ménard (1989). A given number of photons (usually 10^7 for the optically-thin models) are followed as they leave the star and propagate through the dusty envelope. At each scattering event, the new photon path and Stokes intensities are calculated. The density structure of the envelope can be spherically symmetric or axisymmetric (2D) and is specified as a table of grain number density at each point (r, θ), where r is the radial distance from the star and θ is the polar angle ($\theta = 0°$ for a pole-on view and $\theta = 90°$ for an equatorial view). Photons emerging from the nebula are collected in bins according to their polar angle to form a 2-D scattered light image of the nebula for each viewing inclination angle. In practice, these bins are averaged over inclination angle, to improve signal to noise, so that the bin approximating a pole-on view (bin 1) actually encompasses viewing angles in the range $\theta = 0$–$10°$. Since the observations of HD 179821 suggest that the nebula geometry is either spherically symmetric or axisymmetric but viewed pole-on, this bin is used throughout.

The dust-grain model is specified by the refractive index of the dust, m, and the grain-size distribution. We assume a truncated power-law distribution of grain sizes such that the number of grains of size a per unit volume is given by $n(a) = Aa^{-\beta}$ where

Table B1. Optical constants for various materials at $\lambda = 1.2\,\mu$m and $\lambda = 2.2\,\mu$m.

Material	$m(\lambda = 1.2\,\mu\text{m})$	$m(\lambda = 2.2\,\mu\text{m})$	Comment	Reference
Ast Sil	1.71, 0.03	1.71, 0.03	'astronomical silicate'	Draine 1985
$Mg_{0.8}Fe_{1.2}SiO_4$	1.790, 0.103	1.866, 0.052	Fe-rich olivine glass	Dorschner et al. 1995
$Mg_{0.6}Fe_{0.4}SiO_3$	1.640, 0.004	1.620, 0.002	Fe-rich pyroxene glass	Dorschner et al. 1995
$Fe_{0.4}Mg_{0.6}O$	1.95, 0.31	2.15, 0.26	iron-magnesium oxide	Henning et al. 1995
Amor. carbon	2.51, 0.76	2.79, 0.80	amorphous carbon	Preibisch et al. 1993
H_2O ice	1.298, 6.7(−6)	1.262, 2.6(−4)	water ice at 140 K	Warren 1984

Table B2. Scattering properties for power-law size distributions of spherical particles. β is the power-law size-distribution index, $C_{sca}(1.2)$ and $C_{sca}(2.2)$ are the scattering cross-sections at 1.2 and 2.2 μm, $\omega_{1.2}$ and $\omega_{2.2}$ the albedos, $g_{1.2}$ and $g_{2.2}$ the scattering-asymmetry parameters, $P_m(1.2)$ and $P_m(2.2)$ the maximum linear polarizations and $R_{1.2/2.2}$ is the ratio $C_{sca}(1.2)/C_{sca}(2.2)$.

Material	β	$C_{sca}(1.2)$	$C_{sca}(2.2)$	$\omega_{1.2}$	$\omega_{2.2}$	$g_{1.2}$	$g_{2.2}$	$P_m(1.2)$	$P_m(2.2)$	$R_{1.2/2.2}$
Astronomical silicate	6.0	5.27(−16)	9.07(−17)	0.62	0.37	0.34	0.32	75	77	5.81
	5.5	1.02(−15)	2.29(−16)	0.71	0.54	0.41	0.40	63	65	4.47
	5.0	2.15(−15)	6.35(−16)	0.78	0.69	0.47	0.46	50	51	3.39
	4.5	4.88(−15)	1.90(−15)	0.83	0.79	0.52	0.51	35	37	2.57
	3.5	3.02(−14)	1.96(−14)	0.83	0.85	0.60	0.57	<10†	<10†	1.54
$Mg_{0.8}Fe_{1.2}SiO_4$	6.0	5.69(−16)	1.22(−16)	0.36	0.35	0.33	0.31	77	71	4.68
	5.5	1.06(−15)	2.97(−16)	0.45	0.50	0.39	0.38	68	57	3.56
	5.0	2.12(−15)	7.90(−16)	0.54	0.64	0.46	0.43	57	45	2.69
	4.5	4.53(−15)	2.22(−15)	0.59	0.72	0.52	0.47	44	30	2.04
	3.5	2.53(−14)	2.04(−14)	0.64	0.78	0.62	0.53	20	<10	1.24
$Mg_{0.6}Fe_{0.4}SiO_3$	6.0	4.66(−16)	7.61(−17)	0.91	0.87	0.35	0.33	76	78	6.12
	5.5	9.31(−16)	1.98(−16)	0.94	0.94	0.42	0.42	67	64	4.70
	5.0	2.04(−15)	5.75(−16)	0.96	0.97	0.48	0.48	50	53	3.55
	4.5	4.83(−15)	1.80(−15)	0.97	0.98	0.53	0.53	35	39	2.68
	3.5	3.31(−14)	2.06(−14)	0.97	0.99	0.59	0.59	<10†	<10†	1.61
$Fe_{0.4}Mg_{0.6}O$	6.0	6.71(−16)	1.45(−16)	0.20	0.14	0.29	0.27	82	77	4.62
	5.5	1.16(−15)	3.27(−16)	0.26	0.22	0.35	0.33	77	69	3.55
	5.0	2.17(−15)	8.00(−16)	0.33	0.32	0.42	0.39	68	58	2.71
	4.5	4.34(−15)	2.14(−15)	0.39	0.41	0.48	0.44	59	47	2.02
	3.5	2.17(−14)	1.66(−14)	0.47	0.51	0.62	0.54	39	27	1.31
Amorphous carbon	6.0	1.11(−15)	2.16(−16)	0.20	0.11	0.22	0.20	82	81	5.14
	5.5	1.80(−15)	4.50(−16)	0.25	0.17	0.26	0.24	76	73	3.99
	5.0	3.08(−15)	1.01(−15)	0.30	0.24	0.31	0.28	68	66	3.06
	4.5	5.66(−15)	2.42(−15)	0.35	0.32	0.37	0.33	60	48	2.34
	3.5	2.46(−14)	1.71(−14)	0.44	0.44	0.52	0.45	44	42	1.45
H_2O ice	6.0	1.20(−16)	1.56(−17)	1.0	0.90	0.40	0.36	94	97	7.68
	5.5	2.63(−16)	4.30(−17)	1.0	0.95	0.52	0.48	90	94	6.12
	5.0	6.63(−16)	1.37(−16)	1.0	0.98	0.62	0.59	83	90	4.86
	4.5	1.89(−15)	4.80(−16)	1.0	0.99	0.70	0.67	74	85	3.93
	3.5	1.97(−14)	7.11(−15)	1.0	1.0	0.79	0.77	46	72	2.77
$Mg_{0.8}Fe_{1.2}SiO_4$ + H_2O ice	6.0	1.72(−16)	2.68(−17)	0.55	0.43	0.34	0.31	91	90	6.42
	5.5	3.60(−16)	7.29(−17)	0.67	0.62	0.43	0.40	85	84	4.94
	5.0	8.45(−16)	2.23(−16)	0.76	0.78	0.51	0.48	77	77	3.80
	4.5	2.20(−15)	7.41(−16)	0.82	0.86	0.58	0.54	67	68	2.97
	3.5	1.92(−14)	9.58(−15)	0.87	0.92	0.68	0.62	48	47	2.00

† A negatively-polarized back-scattering peak is also produced.

$a_{\rm min} \leq a \leq a_{\rm max}$ and A is a constant defined such that

$$N = A \int_{a_{\rm min}}^{a_{\rm max}} a^{-\beta}\, {\rm d}a \tag{A1}$$

and N is the total number of grains per unit volume, which is given at each (r, θ) position by the density table. The grains are assumed to be spherical and the scattering calculations use Mie theory.

The model geometry suggested by the observations is a hollow shell, with inner radius $r_{\rm in}$ and outer radius $r_{\rm out}$. The number density of dust grains at the inner radius, $r_{\rm in}$, is $N_{\rm in}$, and outside the shell ($r < r_{\rm in}$ and $r > r_{\rm out}$) it is zero. Within the shell, the grain number density is given by the density table. We set the outer shell boundary to 5.4×10^4 AU, corresponding to 9 arcsec at 6 kpc, as indicated by the extent of the scattered light detected by Kastner & Weintraub (1995). The model images at each viewing angle are computed on a 2D grid of 99×99 pixels, with the star at the central pixel. For modelling purposes we have ignored the observed offset of 0.3 arcsec between the star and the centre of the shell. With an outer-shell radius of $r_{\rm out} = 9$ arcsec, a model pixel is equivalent to 0.18 arcsec.

APPENDIX B: SCATTERING PROPERTIES OF VARIOUS DUST-GRAIN MODELS

We list here the results of scattering calculations for various particle-size distributions. All calculation assume Mie scattering and are based on modified versions of the BHMIE and BHCOAT spherical-particle algorithms of Bohren & Huffman (1983). Power-law size distributions (Section 3.1) are used throughout with $a_{\rm min} = 0.05\,\mu$m and $a_{\rm max} = 2.0\,\mu$m. Table B1 lists optical constants at $\lambda = 1.2\,\mu$m and $\lambda = 2.2\,\mu$m for various materials and Table B2 lists their scattering properties.

The albedo, ω, is the ratio of scattering and extinction cross-sections. The asymmetry parameter, g, is the average cosine of the scattering angle and a measure of the forward-throwing nature of the scattering. For a particle that scatters light equally in all directions, $g = 0$, whereas for forward-throwing scattering, g lies in the range $0 < g \leq 1$. More formal definitions may be found in Bohren & Huffman (1983).

This paper has been typeset from a TEX/LATEX file prepared by the author.